

Superradiance in acoustic black hole

Chengye Yu,^{*} Xiaolin Zhang,[†] Sobhan Kazempour,[‡] and Sichun Sun[§]
School of Physics, Beijing Institute of Technology, Beijing, 100081, China

Rotating superradiance in cylindrical geometries has recently been observed experimentally using acoustic waves, shedding light on the superradiant phenomenon in black holes. In this paper, we study superradiance in acoustic black holes made with solid material for the first time, using theoretical analysis and numerical simulations in COMSOL Multiphysics. We find that superradiance can occur in acoustic black holes when the general superradiance condition is met. We also find that the amplification effect is significantly weaker in acoustic black holes than in regular cylinders, due to absorption within the black holes. Furthermore, we have found that different acoustic black hole models exhibit similar superradiance behavior at the same physical scale, which is also consistent with the phenomena in extremal Kerr black holes. We also present that the solid material ABH model has the most degrees of freedom.

I. INTRODUCTION

Dicke [1] proposed the concept of superradiant states [2], attributing its amplification to coherence. In 1969, Roger Pense proposed the energy extraction of a rotational black hole as the early version of the superradiance [3, 4]. Later, Zel'Dovich [5, 6] suggests that superradiance can occur on the surface of rotating objects, where the amplitude of the incident wave is significantly larger than the amplitude of the reflected wave. (The phenomenon of superradiance in black holes has also been extensively studied; see [7–28].) Related experiments are then proposed to detect this phenomenon, especially for rotational superradiance [2, 29–35]. In experiments, rotational superradiance occurs when an object moves around a rotational axis with a specific angular velocity, and the condition for superradiance is

$$\omega - m\Omega < 0, \quad (1)$$

where ω is the incident waves frequency, m , is the azimuthal quantum number with respect to the axis of rotation, and Ω is the angular frequency of the cylinder. Eq. (1) represents the most general condition for superradiance, and it serves as an indicator for determining whether the phenomenon of superradiance occurs [36–41].

It is found that low-frequency sound modes with orbital angular momentum (OAM) [42, 43] are transmitted through an absorbing rotating disk and amplified when the disk rotation rate meets superradiant conditions [44, 45]. This rotational Doppler effect [46, 47] has also been observed in light-carrying OAM that is backscattered from a rotating rough surface, enabling the remote measurement of an object's rotation speed [48–50]. There are other methods to detect superradiance; for example, Teukolsky et al [51] proposed the idea

of creating a "perfect mirror" in a so-called black hole bomb [52–54]. Numerical studies of charged black hole bombs at the linear level in the field amplitude have been conducted in both the frequency and time domains, as in Refs. [15, 55, 56], while analytical studies have been carried out in Refs. [57, 58].

Despite significant progress in the study of superradiance, there remains a lack of understanding of the phenomenon in certain systems, such as the acoustic 'black hole' (ABH). ABHs are systems that mimic the behavior of black holes in general relativity, but in the context of acoustic waves [23, 59–62]. The concept of ABH is derived from the gravitational effects of astronomical black holes [63]. As is widely known, the information that approaches a black hole is absorbed and debatably transmitted outside the black hole in the form of Hawking radiation [64–68]. In engineering, researchers have discovered that altering the surface structure of a solid can cause an elastic wave propagating within it to be absorbed by a wedge structure, producing an effect analogous to the gravitational pull of a black hole. This phenomenon is referred to as ABH structure [69–73]. The study of superradiance in ABHs is important because it can provide insights into black-hole behavior and the radiation emitted by rotating systems.

The paper is organized as follows: In Section II, we introduce the ABH and derive its amplification factor by solving the radial equation subject to the relevant boundary conditions. In Section III, we use semi-analytical and simulation methods in COMSOL Multiphysics [74–76] to validate superradiance conditions and amplification factors. In Section IV, we summarize our main results and discuss the implications of our findings. Finally, in Section V, we establish an analogy between the solid material ABH model and the rotating draining bathtub ABH model, and investigate the resulting superradiance.

II. ACOUSTIC BLACK HOLE SET-UP

The physical structure of two-dimensional ABH is given by [70]. The plate consists of a section with a

^{*} chengyeyu1@hotmail.com

[†] xiaolinzhang66@outlook.com

[‡] sobhan.kazempour1989@gmail.com

[§] sichunssun@gmail.com

constant thickness h_2 extending from R to the edge of the plate, a tapered region (from r_1 to R), and a central plateau from 0 to r_1 with a constant thickness h_1 . The shape is as follows:

$$h(r) = \begin{cases} h_2 & (r \geq R), \\ b(r - r_1)^n + h_1 & (r \leq R). \end{cases} \quad (2)$$

The extreme case with $h_1 = r_1 = 0$ and $n \geq 2$ corresponds to an ideal ABH structure (see Fig. 1). In this paper, we set the following parameters for ABH structure: $b = 7.34 \times 10^{-4} m^{-1}$, $r_1 = 2 \times 10^{-2} m$, $h_1 = 6 \times 10^{-4} m$ and $n = 2$ (correspond to the **Simulation analysis** in Sec. IV), and the superradiance analytical analysis in ABH is derived in Sec. III.

III. SUPERRADIANCE MODE

We start from Kirchhoff's equation [77] for a quiescent inviscid and non-conducting fluid, with the equation of mass conservation $\partial \rho / \partial t + \nabla \rho \mathbf{v} = 0$ and the momentum conservation $\rho \partial \mathbf{v} / \partial t = -\nabla p$. In the air ($r > R$) we have

$$\begin{aligned} i\omega \rho_+ + \rho_0 \nabla \mathbf{v}_+ &= 0, \\ i\omega \rho_0 \mathbf{v}_+ + \nabla p_+ &= 0, \\ p_+ &= c_s^2 \rho_+, \end{aligned} \quad (3)$$

while the ABH is described by the model ($r < R$)

$$\begin{aligned} i\omega \rho_- + \rho_f \nabla \mathbf{v}_- &= 0, \\ i\omega \rho_f \mathbf{v}_- + \nabla p_- &= 0, \\ p_- &= c_{eff}^2 \rho_-, \end{aligned} \quad (4)$$

where R is the radius of ABH. Zel'dovich's original "dynamical" argument [5, 6] follows the Lorentz-invariant Klein-Gordon equation, and through Eq. (3), we have $\square p_+ = 0$ outside the ABH.

In a coordinate system where the medium is at rest, the absorption can be characterized by a parameter α , causing Eq. (4) to become a modified equation

$$\square p_- = \frac{\alpha}{c_{eff}^2} \partial_t p_- \quad (5)$$

We reconsider the wave equation (3) outside the ABH in cylindrical coordinates, and the radial equation reduces exactly to

$$\frac{1}{r} \frac{\partial}{\partial r} \left(r \frac{\partial p_+(r)}{\partial r} \right) + \left[\frac{\omega^2}{c_s^2} - \frac{m^2}{r^2} \right] p_+(r) = 0. \quad (6)$$

Dissipation is essential for the generation of the superradiance. In the rotating coordinate system, $\alpha(\omega - m\Omega)$ replaces $\alpha\omega$ under the superradiation condition, meaning that the absorption term becomes an amplification term, allowing superradiance to occur [2]. Inside the ABH, the

wave equation (5) can be rewritten in the more convenient form

$$\frac{1}{r} \frac{\partial}{\partial r} \left(r \frac{\partial p_-(r)}{\partial r} \right) + \left[\frac{\kappa^2}{c_{eff}^2(r)} - \frac{m^2}{r^2} \right] p_-(r) = 0, \quad (7)$$

where

$$\kappa = \sqrt{\omega^2 + i\alpha(\omega - m\Omega)}, \quad c_{eff}(r) = \sqrt{c_s^2 - v^2(r)}, \quad (8)$$

where κ is the complex angular frequency. The ABH contains an effective complex sound velocity $c_{eff}(r)$ (where c_s is the sound speed) relative to the radial distance r , with $v(r)$ representing the background flow rate[59]. The solution to Eq. (6) is the combination of Bessel functions,

$$p_+(r) = C_1 J_m(\omega r / c_s) + C_2 Y_m(\omega r / c_s), \quad (9)$$

where the coefficients C_1 and C_2 are related to the incident (reflected) part with amplitude for outside ABH. It is worth noting that ω / c_s is the number of sound waves outside ABH. It is evident that the solution to Eq. (7) depends on the background flow rate $v(r)$. Notably, whether the background flow rate is constant or not significantly influences the internal solutions of the ABH. Therefore, this aspect will be the focus of discussion in the next section.

Before working out explicitly the case of a rotating object in (r, φ, z) spatial coordinates with a dissipative surface at $r = R$, we need consider a small quantity ε relative to R that outside surface R_+ is $R + \varepsilon$ and inside surface R_- is $R - \varepsilon$. Obviously, in Fig. 2, a discontinuity exists between the outer surface R_+ and the inner surface R_- , requiring continuity conditions to ensure smoothness on the scattering surface. We consider matching the pressure and velocity of the internal and external solutions under the jump condition of $r = R$ [78]. From the continuity of velocity ($\mathbf{v}_+ = \mathbf{v}_-$) in Eqs. (3), (4), we can get

$$\frac{\partial p_+(r)}{\partial r} \Big|_{r=R_+} = \frac{\rho_0}{\rho_f} \frac{\partial p_-(r)}{\partial r} \Big|_{r=R_-}. \quad (10)$$

We can define the impedances inside and outside the ABH. Since sound scattering occurs at the boundary of the ABH, we assume the small quantity is negligible, allowing us to obtain the associated impedance as

$$Z_+ = \rho_0 c_s, \quad Z_- = \rho_f c_{eff}(r) \Big|_{r=R_-} = \rho_0 c_s Z, \quad (11)$$

where Z_+ is the outside impedance, Z_- is the inside impedance, and Z is the characteristic acoustic impedance of the fibrous material[79] (see Fig. 2).

Due to the mismatch in acoustic impedance between the external and internal environments, the incident wave encounters inside impedance conditions at the scattering interface $r = R$. In terms of impedance, the boundary condition for both sound and surface waves in the rest frame of ABH is

$$p_+(R_+) - p_-(R_-) = -\frac{Z_-}{i\rho_0 \omega} \frac{\partial p_+(r)}{\partial r} \Big|_{r=R_+}. \quad (12)$$

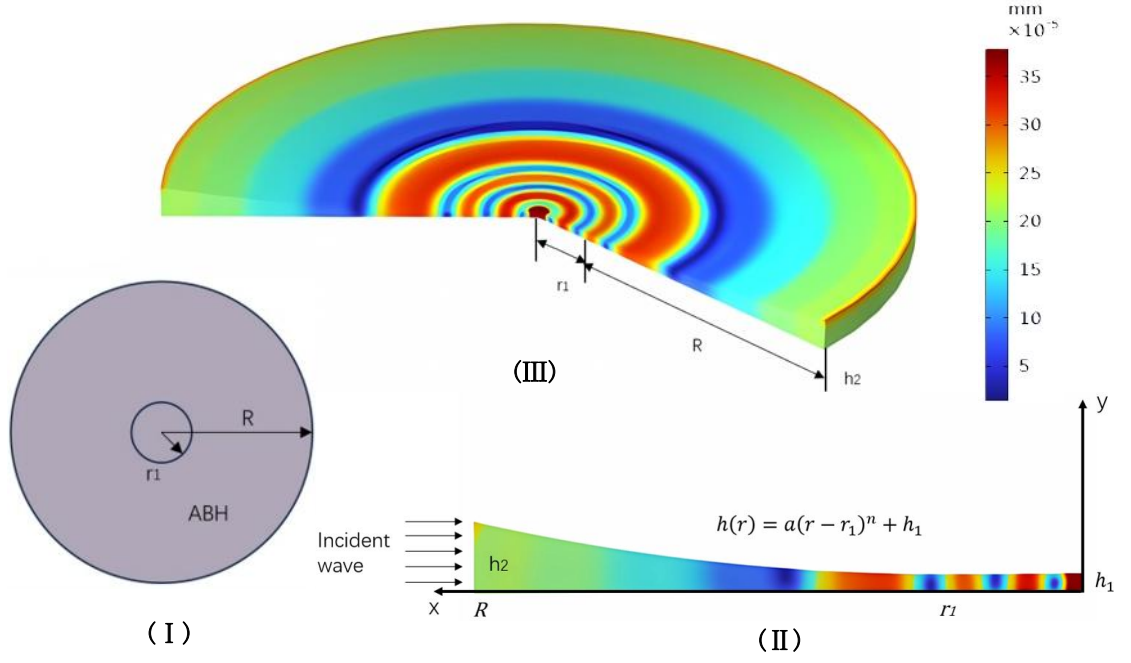


FIG. 1. (I) Sketch of a top view of ABH. (II) A slice view of two-dimensional ABH simulated by COMSOL. (III) 3D view of ABH. Color scheme: Range of displacement induced by a $1Pa$ point load applied at the boundary of the ABH, where the simulation is transient and the azimuthal mode number $m = 0$.

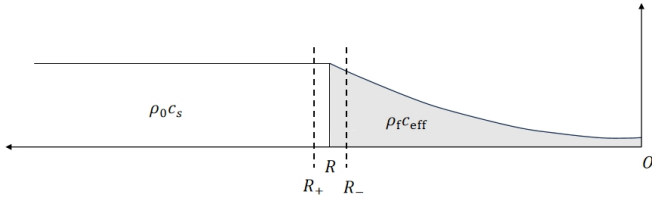


FIG. 2. Outside impedance and inside impedance of the ABH.

When the object rotates uniformly with angular velocity Ω , it is sufficient to transform to a new angular coordinate $\tilde{\phi} = \phi + \Omega t$, which effectively amounts to the replacement of ω with $\omega - m\Omega$ in Eq. (12). Then the inside impedance condition (12) becomes

$$p_+(R_+) - p_-(R_-) = -\frac{Z_-}{i\rho_0(\omega - m\Omega)} \frac{\partial p_+(r)}{\partial r} \Big|_{r=R_+}. \quad (13)$$

Then through Eq. (10), (13), the relationship between coefficients C_1 and C_2 is

$$\frac{C_1}{C_2} = -\frac{\tilde{Z}Y'_m(\omega R_+/c_s) - Y_m(\omega R_+/c_s)}{\tilde{Z}J'_m(\omega R_+/c_s) - J_m(\omega R_+/c_s)}, \quad (14)$$

where

$$\tilde{Z} = Z\left(\frac{\omega}{c_{eff}(r)} \frac{p_-(r)}{\partial_r p_-(r)} \Big|_{r=R_-} - \frac{\omega}{i(\omega - m\Omega)}\right), \quad (15)$$

where $'$ means derivative with respect to the argument. The relationship between the reflected (incident) part with amplitude and coefficients C_1 , C_2 is $C_1 - iC_2$ ($C_1 + iC_2$). For simplicity, letting $C = C_1/C_2$, and amplification factor can be written as

$$\rho = \left| \frac{C - i}{C + i} \right|^2 - 1. \quad (16)$$

One of the conditions for rotational superradiance is $\omega - m\Omega$, where the superradiant phenomenon occurs on the radiating surface of the cylinder, that is, $\rho > 0$. It is worth mentioning that if the cylinder is conventional and not ABH inside, then the amplification factor (16) is different, which we will discuss more in the section IV.

IV. SEMI-ANALYTICAL AND SIMULATION ANALYSIS

In this section, we perform semi-analytical and COMSOL simulations to study the superradiance relation of the sound wave angular frequency and cylinder/ABH angular velocity. The two methods obtain amplification factors for a cylinder and ABH, respectively, and agree well. First, we provide a brief overview of the analytical methods to ensure consistency between the theoretical and simulation analyses.

Semi-analytical analysis: We use Eq. (16) to calculate amplification factor, for semi-analytical calculation

Simulation analysis: In this paper, COMSOL software is used to simulate the acoustic superradiant phenomenon occurring in a fluid domain, and the amplification factor ρ_s of the cylinder or ABH is obtained by setting appropriate boundary conditions with the pressure acoustic module and Delany-Bazley-Miki model [79, 80]. The amplification factor ρ_s is the ratio between the background sound pressure level and the scattered sound pressure level.

Settings: The values of the parameter in Eq. (16) are fixed as: the density of air is $1.2kg/m^3$, the sound speed of air c_s is $343m/s$, the radius of the cylinder R is $10^{-1}m$ and the azimuthal quantum number is $m = 1$. The value of the sound absorption parameter α does not impact much on the superradiant intensity. For simplicity we set $\alpha = 0s^{-1}$. Other parameters are mentioned in section II.

When the background fluid rate $v(r)$ is constant, Eq. (7) is just the inner solution of the cylinder, and its solution can also be expressed as the Bessel function

$$p_-(r) = C_3 J_m(\kappa r / c_{eff}), \quad (17)$$

When the background fluid rate changes, if we assume that the rate $v(r)$ changes gently with radial r , then approximated by WKB, the internal solution of the ABH is

$$p_-(r) \sim \frac{1}{\sqrt[4]{rc_{eff}(r)}} \exp(i \int \frac{\kappa}{c_{eff}(r)} dr). \quad (18)$$

The characteristic acoustic impedance of the fiber material is

$$Z = 1 + A_1 X^{-A_2} - iA_3 X^{-A_4}, X = \rho_0 \omega / (2\pi \varpi), \quad (19)$$

where ϖ is the flow resistance of the material, ρ_0 is the air density. For the small frequency that $X \leq 0.025$, we can use the values below. We mainly examine glass fiber and rock materials, with their specific acoustic impedance parameters shown in Table I.

TABLE I. Characteristic acoustic impedance for Miki and low-frequency Glass (Rock) fiber.

Materials[81]	X	A_1	A_2	A_3	A_4
Miki	< 1	0.079	0.632	0.12	0.632
Low Glass fibre(LG)	≤ 0.025	0.0688	0.707	0.196	0.549
Low Rock fibre(LR)	≤ 0.025	0.081	0.699	0.191	0.556

TABLE II. The different values of flow resistances we used in the plot.

Flow resistance (ϖ)	ϖ_0	ϖ_1	ϖ_2	ϖ_3
Value ($Pa \cdot s/m^2$)	$2.5 * 10^3$	$1 * 10^4$	$2 * 10^4$	$5 * 10^4$

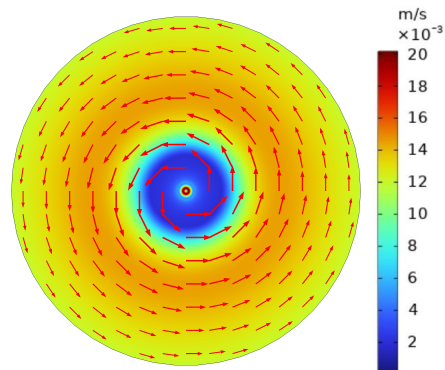


FIG. 3. The distribution of a sound field in an ABH where the frequency of the sound wave is $100Hz$ and the angular velocity of the ABH is $0rad/s$. Color scheme: Range of transient sound speed induced by the specified acoustic pressure field

It is worth mentioning that two conditions are essential: the first is the impedance of the fibrous material attenuation term Z , and the second is the superradiant condition $\omega - m\Omega < 0$, which determines whether the superradiance can occur.

A. Simulation of acoustic superradiation in a fluid domain

1. Sound field ABH in the non-rotational case

This section investigates the sound field distribution of ABHs in a fluid domain. First, we analyze the sound-field distribution in a static fluid domain, before extending the study to a rotating fluid domain.

Fig. 3 illustrates the distribution of sound waves with an azimuth mode $m = 1$ within an ABH in a quiescent flow field. The fluid flow field comprises both angular and radial velocity components, characterized by the azimuthal number m . The effect of the acoustic black hole is that the sound speed decreases towards the singularity. Notice the artifact we put in by hand near the center plateau region in this simulation.

2. Rotational Superradiance

The key to acoustic superradiation is the superradiation condition, where the relation of the angular frequency ω and rotational frequency Ω enables superradiation amplification. In this section, the angular velocity of the acoustic black hole is set to be $200\pi rad/s$ with different incident sound wave frequencies.

Fig. 4 illustrates the non-superradiation case. In this case, the sound waves tend to converge at the black hole's 'event horizon' rather than its 'singularity', dividing the sound field into three regions: the outer high-velocity region (near the 'event horizon'), the middle medium-

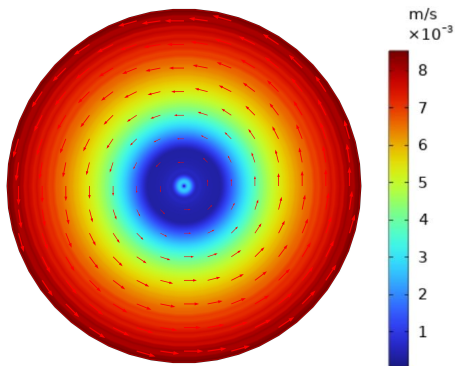


FIG. 4. The distribution of a sound field in an ABH where the frequency of the sound wave is 200Hz , and the angular velocity of the ABH is $200\pi\text{rad/s}$. Color scheme: range of transient sound speed induced by the specified acoustic pressure and the rotation.

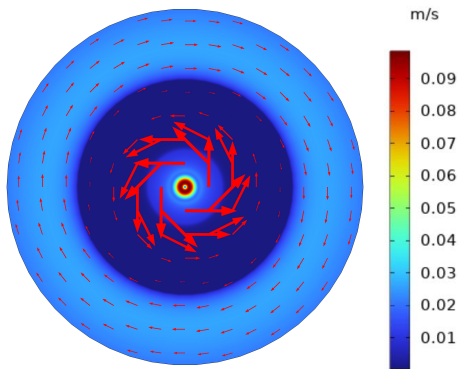


FIG. 5. The distribution of a sound field in an ABH where the frequency of the sound wave is 20Hz , and the angular velocity of the ABH is $200\pi\text{rad/s}$. The propagation direction of sound waves is in the radial direction of the ABH. Color scheme: Range of transient sound speed induced by the specified acoustic pressure field and the rotation.

velocity region, and the inner low-velocity region (near the ‘singularity’). We can see the radial rotational effect in this plot compared to the static Fig.3.

Fig. 5 satisfies the superradiation condition, and it has instability in the fluid domain. In the radial direction, the sound wave propagates outward in some region, effectively indicating that the superradiation condition $\omega - m\Omega$ replaces the inherent angular frequency ω of the sound wave. This observation is critical in detecting the amplification effect of acoustic superradiation and provides a foundation for future experimental observations of superradiation phenomena.

B. Superradiance for ABH

Unlike the amplification factor ρ of the semi-analytical analysis, the amplification factor of the COMSOL simu-

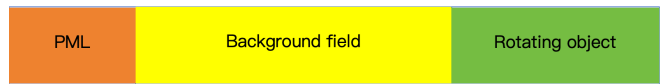


FIG. 6. The main components of the simulation. PML: Absorbs the outgoing waves and monitors the intensity of the scattered waves. Background field: Provides the incident wave and is the region where superradiance occurs. Rotating object: Superradiance object.

lation can be written as

$$\begin{aligned} L_{p,s} - L_{p,b} &= 20\log_{10}\left(\frac{p_s}{p_{ref}}\right) - 20\log_{10}\left(\frac{p_b}{p_{ref}}\right) \\ &= 20\log_{10}(R_{s,b}) \end{aligned} \quad (20)$$

where $L_{p,s}$ is the scattering sound pressure level and $L_{p,b}$ is the background sound pressure level. $R_{s,b}$ represents the reflection coefficient, and the reference sound pressure $p_{ref} = 20\mu\text{Pa}$. In the simulation, with an incident wave amplitude of 1Pa in air, the background sound pressure level $L_{p,b}$ is measured at 90.969dB .

The main components of the simulation and their respective functions are depicted in Fig. 6. Absorption and superradiant amplification in an ABH are competing mechanisms in both semi-analytical and simulation. In Fig. 7, we can see the different amplification factors (defined differently) obtained from the theoretical semi-analytical study and simulation. The Delany-Bazley-Miki model was used to describe the acoustic impedance of fiber materials. This model better captures the frequency-dependent dissipation in real materials, resulting in stronger absorption. The actual acoustic impedance of the surface fiber layer failed to reach the theoretically assumed optimal value that maximizes absorption. Theoretically, in an ideal ABH, virtually all the incident wave energy is absorbed, with only a negligible portion being reflected. However, in practical implementation/simulation, the ABH tip cannot be infinitely sharp and is inevitably truncated, resulting in a small flat plateau Eq.2, which substantially diminishes the efficiency of energy trapping and dissipation. More incident wave energy is reflected rather than absorbed. When this part of the reflected wave meets the hyperradiative condition at the rotational boundary, it can extract energy from the rotation of the system. Ultimately, the observed superradiation amplification factor appears to far exceed the semi-analytical factor in numerics in Fig 7.

Fig. 7 shows that when the impedance Z changes with increasing flow resistance of the fiber material, the amplification factor decreases. This suggests that the fiber’s material properties significantly affect the superradiant phenomenon. Furthermore, ABH exhibits strong absorption due to its gradient thickness profile $h(r)$ and viscoelastic material losses. This absorption suppresses wave magnification in the ABH to approximately two-thirds of the value observed in a conventional cylinder. It also suggests that when the flow resistance of the fiber material becomes sufficiently large, the observation of su-

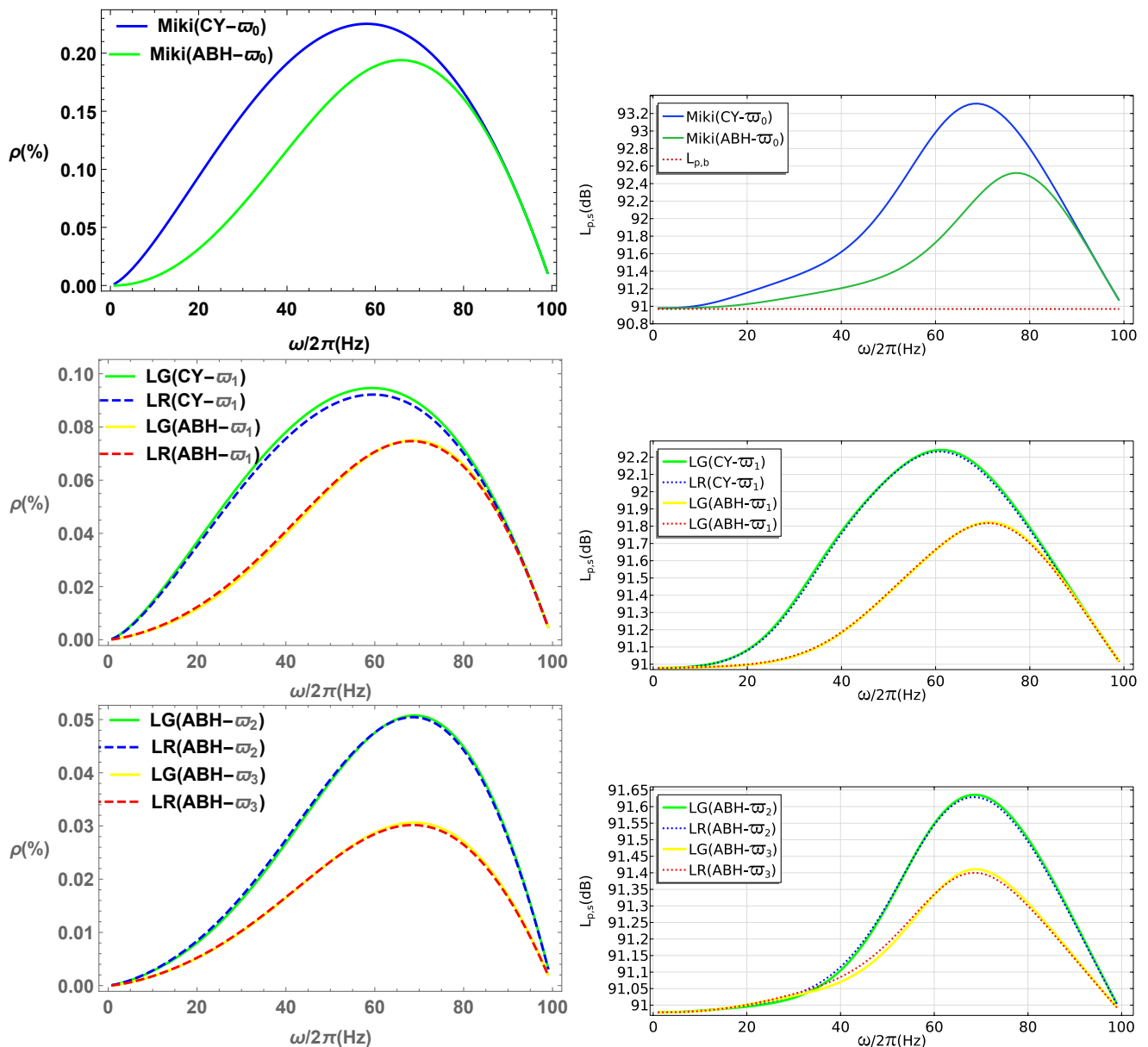


FIG. 7. The left figures show the amplification factor ρ under semi-analytical analysis, and the right figures show the pressure level $L_{p,s}$ under simulation. CY stands for cylindrical structure, and ABH stands for ABH structure.

perradiance can be considerably challenging.

Unlike a regular cylinder, ABH exhibits a strong absorption effect, causing the sound waves to be largely trapped within ABH. This phenomenon is clearly illustrated in Fig. 7, and the ABH internal structure causes the absorption of sound waves in the simulation. For a regular cylinder, the amplification factors are similar to the results of V. Cardoso et al[2, 30].

V. SUPERRADIANCE FOR ANALOGUE BLACK HOLE

In this section, we study a different analogue black hole model: a draining bathtub fluid flow with a sink at the origin, firstly introduced by Visser [59]. The superradiance of this kind of analogue black hole has been studied in previous works [60, 62]. Interestingly, Ref. [23] considered varying water depth and describes a more realistic draining geometry. In our Chapter V A, the rotating draining bathtub model is studied with the same parameter range as the solid material ABH, and the superradiance condition was derived. Chapter V B employs Eq. 30 to compare the superradiance intensity across an

identical parameter range. In Chapter VC, we present Tab. IV to make analogies and summaries of the superradiance theoretical models: the solid material ABH, the draining bathtub, and the Kerr black hole.

At last, we conclude that across these three models, although the superradiance behavior is similar, the solid material ABH has the most degrees of freedom.

A. Rotating draining bathtub ABH

In this section, we review the basic setup of the draining bathtub model [23]. The event horizon is defined as the surface where the radial velocity equals the propagation speed

$$\bar{c}_{\text{gw}}^2 = \bar{v}_r^2. \quad (21)$$

Here, we further normalize the gravitational wave velocity and the radial velocity as $\bar{c}_{\text{gw}} = c_{\text{gw}}/(\sqrt{g\mathbf{h}_\infty})$ and $\bar{v}_r = v_r/(\sqrt{g\mathbf{h}_\infty})$, so that we can directly obtain the dimensionless event horizon. g is the gravitational acceleration and \mathbf{h}_∞ is the water depth. The wave equation around our analogue black hole can be written as

$$\frac{d^2 H(\bar{r}_*)}{d\bar{r}_*^2} + \bar{V}(\bar{r})H(\bar{r}_*) = 0, \quad (22)$$

where

$$\begin{aligned} \bar{V}(\bar{r}) = & \frac{1}{\bar{g}\mathbf{h}}(\sigma\bar{\omega} - \sqrt{2}\frac{m\bar{B}}{\bar{r}^2})^2 + \frac{1}{2}\left(\frac{(\bar{\mathbf{h}}\bar{r})_{,\bar{r}}}{\bar{\mathbf{h}}\bar{r}}\right)\left(\frac{\Delta_{,\bar{r}}}{\Delta^3}\right) \\ & - \frac{m}{\Delta\bar{r}^2} - \frac{1}{\Delta^2}\left[\frac{1}{4}\left(\frac{(\bar{\mathbf{h}}\bar{r})_{,\bar{r}}}{\bar{\mathbf{h}}\bar{r}}\right)^2 + \frac{1}{2}\left(\frac{(\bar{\mathbf{h}}\bar{r})_{,\bar{r}}}{\bar{\mathbf{h}}\bar{r}}\right)_{,\bar{r}}\right], \end{aligned} \quad (23)$$

and its solution is

$$H \sim \begin{cases} \exp(-i\sigma\bar{\omega}\bar{r}_*) + \mathcal{R}\exp(i\sigma\bar{\omega}\bar{r}_*), & \bar{r} \rightarrow \infty, \\ \mathcal{T}\exp(-i\frac{1}{\sqrt{g\mathbf{h}_H}}(\sigma\bar{\omega} - \frac{\sqrt{2}m\bar{B}}{\bar{r}_H^2})\bar{r}_*), & \bar{r} \rightarrow \bar{r}_H. \end{cases} \quad (24)$$

Using boundary conditions (24), we find the following ‘‘energy conservation’’ condition

$$1 - |\mathcal{R}|^2 = \frac{1}{\sqrt{g\mathbf{h}_H}}\left(1 - \frac{\sqrt{2}m\bar{B}}{\sigma\bar{\omega}\bar{r}_H^2}\right)|\mathcal{T}|^2, \quad (25)$$

and superradiance occurs whenever

$$0 < \sigma\bar{\omega} < \frac{\sqrt{2}m\bar{B}}{\bar{r}_H^2}, \quad (26)$$

where $\bar{\omega} = \omega/(\sigma\sqrt{g\mathbf{h}_\infty})$ and σ is a constant. $\bar{A} = A/(\mathbf{h}_\infty\sqrt{2g\mathbf{h}_\infty})$ and A is related to the radial flow velocity. $\bar{B} = B/(\mathbf{h}_\infty\sqrt{2g\mathbf{h}_\infty})$ and B is related to the angular flow velocity. Other dimensionless parameters are $\bar{r}_H = r_H/\mathbf{h}_\infty$, $\bar{\mathbf{h}}_H = \mathbf{h}_H/\mathbf{h}_\infty$ and $\bar{g} = \tilde{g}/g$ (\tilde{g} can be found in Ref. [23]).

Eq. (26) effectively rescales the parameters and variables. Provided that it is consistent with the superradiance condition given by Eq. (1), the superradiance condition can be more intuitively expressed as

$$0 < \tilde{\omega} < m\bar{\Omega}_H, \quad (27)$$

where $\tilde{\omega} = \bar{\omega}/(\sqrt{2}/\sigma)$. All parameters and functions adhere to the conventions established in Ref. [23], with the exception that we adopt the notation \mathbf{h} for the free-surface function to avoid ambiguity (\mathbf{h}_H represents the water depth at the event horizon.).

B. Numerical analysis

Next, we will work with two distinct dimensionless parameters, which allow for a natural and immediate comparison with the Kerr black hole scattering, namely the normalized rotational flow velocity evaluated at the event horizon

$$\bar{v}_\phi = \frac{\bar{B}}{\bar{r}_H}, \quad (28)$$

and the scaled surface gravity

$$\bar{\kappa}_H = \frac{1}{2}\frac{d}{d\bar{r}}\left(\bar{g}\bar{\mathbf{h}} - 2\left(\frac{\bar{A}}{\bar{r}\bar{\mathbf{h}}}\right)^2\right). \quad (29)$$

To facilitate an analogy with the solid material ABH model under investigation II, we begin by defining the configuration of a rotating draining bathtub ABH, that is

$$\mathbf{h}_\infty \rightarrow h_2, \quad r_H \rightarrow R, \quad (30)$$

where the normalized event horizon is defined as $\bar{r}_H = r_H/\mathbf{h}_\infty$. According to Eq. (30), its value tends to 18.87647. Therefore, the normalized event horizon \bar{r}_H , linear velocity \bar{v}_ϕ , and surface gravity $\bar{\kappa}_H$ are computed by varying the normalized parameters \bar{A} and \bar{B} according to Eqs. (21), (28), (29), and are presented in Table III. **Parameter Settings:** Gravitational acceleration $g = 9.8m/s^2$, a tiny offset near the event horizon $\epsilon = 10^{-10}m$, and the far-field position $r_{max} = 10^2m$. In addition, the factor σ is fixed at 0.3.

Table III shows that when the normalized parameter \bar{A} is fixed, both \bar{r}_H and \bar{v}_ϕ exhibit a positive correlation with \bar{B} , whereas $\bar{\kappa}$ exhibits a negative correlation. The distinction is that, at fixed normalized parameter \bar{B} , only \bar{r}_H exhibits a positive correlation with \bar{A} , in contrast to \bar{v}_ϕ and $\bar{\kappa}_H$, which exhibit a negative correlation. A similar pattern is also observed in the reflectivity described by Eq. (25), which is illustrated in Fig. 8.

C. Analysis and comparison

Fig. 8 indicates that the maximum reflectivity $|\mathcal{R}|_{max}^2$ of the rotating draining bathtub ABH model exhibits

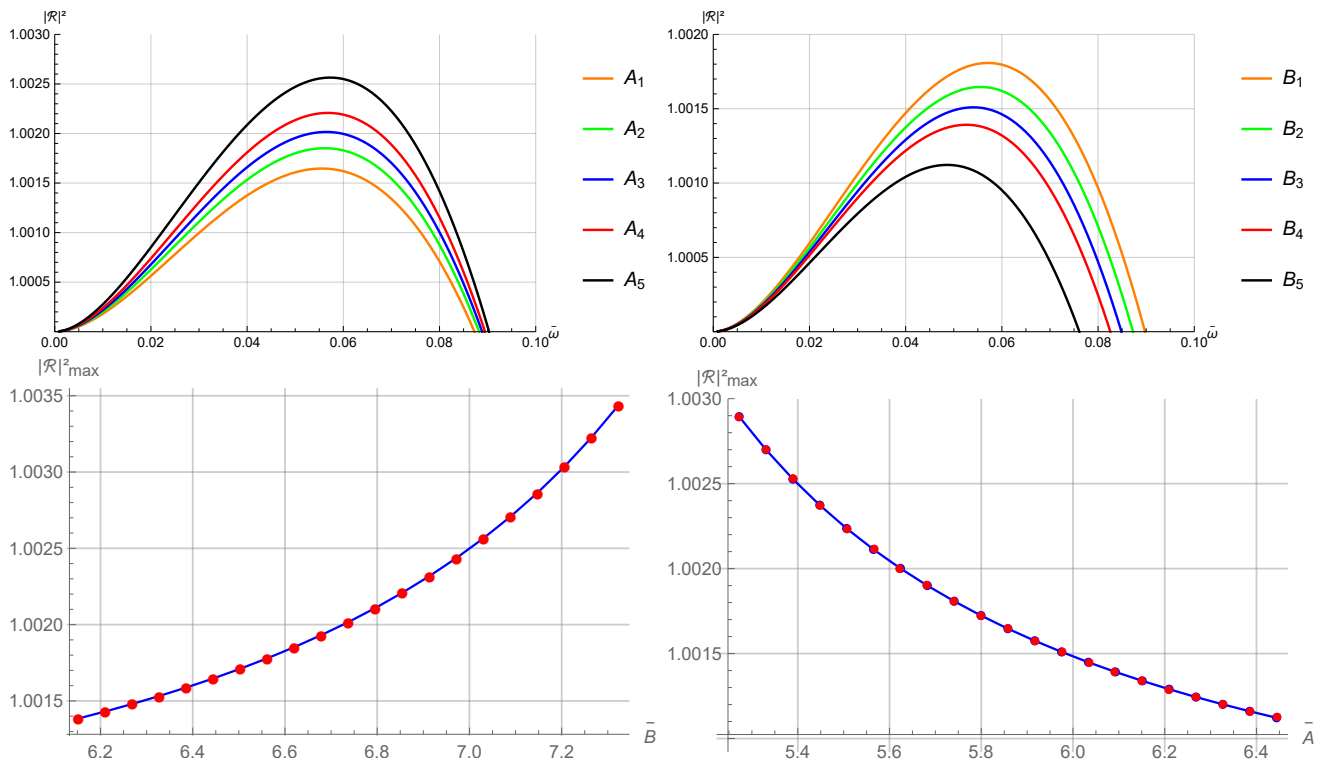


FIG. 8. The top two figures illustrate the variation of the reflectivity $|\mathcal{R}|^2$ with normalized angular frequency $\bar{\omega}$, with parameters \bar{A} and \bar{B} held constant. Correspondingly, the bottom two figures show the maximum reflectivity $|\mathcal{R}|_{max}^2$ as a function of the normalized parameter \bar{B} (\bar{A}).

TABLE III. The different values of \bar{r}_H , \bar{v}_ϕ and $\bar{\kappa}_H$ by changing \bar{B} , with fixing \mathbf{h}_∞ and \bar{A} .

No.	\mathbf{h}_∞ (m)	\bar{A}	\bar{B}	\bar{r}_H	\bar{v}_ϕ	$\bar{\kappa}_H$
A_1	h_2	5.85805	6.44386	18.65709	0.34538	0.91128
A_2			6.61960	18.80489	0.35202	0.91105
A_3			6.73676	18.90434	0.35636	0.91088
A_4			6.85392	19.00451	0.36065	0.91069
A_5			7.02966	19.15605	0.36697	0.91038
B_1		5.74089		18.39565	0.35029	0.91977
B_2		5.85805		18.65709	0.34538	0.91128
B_3	h_2	5.97521	6.44386	18.91944	0.34060	0.90301
B_4		6.09237		19.18267	0.33592	0.89494
B_5		6.44386		19.97749	0.32256	0.87189

a positive correlation with the normalized parameter \bar{B} and a negative correlation with the normalized parameter \bar{A} , when the other parameter is fixed. When the water depth \mathbf{h}_∞ and event horizon of the rotating draining bathtub ABH model approach the settings of the solid material ABH model, the superradiant amplification factor reaches approximately 0.2%—a value of the same order of magnitude as the superradiance intensity in Fig. 7. The parameter A governs the radial flow velocity, analogous to the effective sound speed in the solid material ABH model. An increase in \bar{A} diminishes the superradiance intensity, consistent with the suppression observed

in Fig. 7.

In contrast to Eq. (1), Eq. (26) shows that the range of normalized angular frequencies $\bar{\omega}$ over which superradiance occurs is governed by the normalized event horizon \bar{r}_H and the normalized parameter \bar{B} . Compared to the solid material ABH model and rotating draining bathtub ABH model studied in sections II and V, the superradiative conditions in Kerr black holes are different from the former and can be written as [35]

$$0 < \omega < \frac{ma}{2Mr_+}. \quad (31)$$

To compare all those models, we put out Tab. IV. The largest possible amplification occurs when the Kerr black hole approaches extremality, i.e., $a/M \rightarrow 1$. For the rotating draining bathtub ABH model, on the other hand, the maximum is attained at a sub-critical value $\bar{v}_\phi \approx 0.8$ [23]. In the context of scalar perturbations of a nearly extremal Kerr black hole, we find that the $l = m = 2$ mode exhibits a maximum amplification coefficient of 0.2% [35]. It has also been shown that the maximum possible amplification is 0.3% for scalar waves [52].

For angular velocities near the critical value, the rotational draining bathtub ABH model can achieve a maximum amplification of 35% [23] when we fix $\bar{v}_\phi = 0.8$ and $\bar{\kappa}_H = 1.2$ and vary the depth and radius. This value is higher than the peak magnification of 21.2% predicted by Berti's ideal-fluid model with different parameters for the

TABLE IV. Parameters and analogies across the solid material ABH structure model, Rotational draining bathtub ABH, and Kerr black hole for superradiance.

Description	Theoretical Models				Analogy
	Model I ABH structure model (Sec. IIII)	Model II Rotational draining bathtub ABH		Model III Kerr black hole [35]	
		II.1 Scaling [23]	II.2 Re-scaling V		
Radial coordinate	r	r	\bar{r} $= r/h_\infty$	r	I & II.1 SI units II.2 no units III Geometrized units ($G = c = 1$)
Event horizon	R	r_H	\bar{r}_H	r_+	I & II.1 Consistent scale (Eq. (30)) II & III
Surface gravity	/	κ_H	$\bar{\kappa}_H$	κ_+	Describe the ‘strength’ of the horizon
Angular frequency	ω	ω	$\bar{\omega}$ $= \omega/\omega_{disp}$	ω	II.2 $\omega_{disp} = \sigma\sqrt{g/h_\infty}$ II & III
Angular velocity	Ω	Ω_H $= B/r_H^2$	$\bar{\Omega}_H$ $= \bar{B}/\bar{r}_H^2$	Ω_+ $= a/(2Mr_+)$	Determined by the rotation parameter I & II & III
Condition	$\omega < m\Omega$	$\omega < m\Omega_H$	$\bar{\omega} < m\bar{\Omega}_H$	$\omega < m\Omega_+$	Consistent superradiance conditions
Wave velocity	c_s	c_∞ $= \sqrt{g h_\infty}$	1	1	I & II & III Constant wave speed at infinity
Radial velocity	$v(r)$	v_r $= A/r_H$	\bar{v}_r $= \bar{A}/\bar{r}_H$	/	I & II Can reduce the intensity of superradiance (Fig. 7 8)
Axial velocity	$\Omega * R$	v_ϕ $= B/r_H$	\bar{v}_ϕ $= \bar{B}/\bar{r}_H$	a/M	I & II & III Determine superradiance range
Potential function	/	Eq. (35) in Ref.[23]	$\bar{V}(\bar{r})$	Eq. (3) in Ref.[35]	II & III Similar asymptotic behavior (Infinity: $V \propto \omega^2$, Event horizon: $V \propto (\omega - m\Omega)^2$) I & II & III
Control factors	(Ω, v, Z)	(Ω_H, v_r)	$(\bar{\Omega}_H, \bar{v}_r)$	Ω_+	Angular velocity controls superradiance range(intensity) I & II Radial velocity weaken superradiance I
Superradiance (Current value setting)		$\sim 0.2\%$			I & II & III Impedance controls intensity Can reach the same order of superradiance magnitude

rotational parameter $B = 1$ ($m = 1$) [60]. While the rotational parameter B in the “draining bathtub” model has no theoretical upper bound, experimental realizations require $B \ll B_{max}$ due to fluid dynamic constraints.

VI. CONCLUSION

In conclusion, our analysis has provided a first understanding of the superradiant mode in the solid material ABHs. By examining the radial equations of ABH both inside and outside the boundary, we derive the superradiant mode formulas. Our results reveal that the internal structure of ABH significantly weakens superradiant amplification compared to a regular cylinder, due to its sound-absorbing properties. In addition, the relation of sound-wave frequency and angular velocity is investigated in simulations, and the generation of the superradiant mode in acoustic black holes is demonstrated. This study also demonstrates the importance of the fiber ma-

terial’s properties in generating the superradiant mode, and further research is needed to fully understand the properties of different materials. Our study has important implications for the superradiant experiments. We can observe the superradiant phenomenon by selecting appropriate acoustic materials and optimizing experimental conditions. Moreover, the solid material ABH model and rotating draining bathtub ABH model show superradiance of the same magnitude at the same physical scales, aligning with extremal Kerr black hole predictions. Moreover, the solid material ABH has the most degrees of freedom. This result offers a key theoretical framework for clarifying the fundamental mechanism of superradiance in GR black holes. In summary, the combination of semi-analytical and simulation methods has allowed us to have a deeper understanding of the superradiant phenomenon in ABHs and its comparison with a regular cylinder. Our results have important implications for the experimental detection of the superradiant effect and provide valuable guidance for future research in this area.

-
- [1] R. H. Dicke, Coherence in spontaneous radiation processes, *Phys. Rev.* **93**, 99 (1954).
- [2] R. Brito, V. Cardoso, and P. Pani, *Superradiance*, Vol. 906 (2015).
- [3] R. Penrose, Gravitational Collapse: the Role of General Relativity, *Nuovo Cimento Rivista Serie* **1**, 252 (1969).
- [4] R. Penrose, *Gen. Relat. Gravit.* **34**, 1141 (2002).
- [5] Y. B. Zel’Dovich, Amplification of Cylindrical Electromagnetic Waves Reflected from a Rotating Body, *JETP* **35**, 1085 (1972).
- [6] Y. B. Zel’Dovich, Generation of Waves by a Rotating Body, *JETP Letters* **14**, 180 (1971).
- [7] S. Hod, The superradiant instability regime of the spinning Kerr black hole, *Phys. Lett. B* **758**, 181 (2016).
- [8] A. Arvanitaki, S. Dimopoulos, S. Dubovsky, N. Kaloper, and J. March-Russell, String axiverse, *Phys. Rev. D* **81**, 123530 (2010).
- [9] A. Arvanitaki and S. Dubovsky, Exploring the string axiverse with precision black hole physics, *Phys. Rev. D* **83**, 044026 (2011).
- [10] N. Andersson and K. Glampedakis, Superradiance Resonance Cavity Outside Rapidly Rotating Black Holes, *Phys. Rev. Lett.* **84**, 4537 (2000).
- [11] V. Cardoso and Ó. J. Dias, Small Kerr anti-de Sitter black holes are unstable, *Phys. Rev. D* **70**, 084011 (2004).
- [12] H. Witek, V. Cardoso, A. Ishibashi, and U. Sperhake, Superradiant instabilities in astrophysical systems, *Phys. Rev. D* **87**, 043513 (2013).
- [13] V. M. Mehta, M. Demirtas, C. Long, D. J. E. Marsh, L. McAllister, and M. J. Stott, Superradiance in string theory, *JCAP* **2021** (7), 033.
- [14] M. Baryakhtar, R. Lasenby, and M. Teo, Black hole superradiance signatures of ultralight vectors, *Phys. Rev. D* **96**, 035019 (2017).
- [15] J. C. Degollado, C. A. R. Herdeiro, and H. F. Rúnarsson, Rapid growth of superradiant instabilities for charged black holes in a cavity, *Phys. Rev. D* **88**, 063003 (2013).
- [16] J. C. Degollado, C. A. R. Herdeiro, and E. Radu, Effective stability against superradiance of Kerr black holes with synchronised hair, *Phys. Lett. B* **781**, 651 (2018).
- [17] R. Brito, V. Cardoso, and P. Pani, Black holes as particle detectors: evolution of superradiant instabilities, *Class. Quant. Grav.* **32**, 134001 (2015).
- [18] S. Ghosh, E. Berti, R. Brito, and M. Richartz, Follow-up signals from superradiant instabilities of black hole merger remnants, *Phys. Rev. D* **99**, 104030 (2019).
- [19] M. Casals, S. Dolan, P. Kanti, and E. Winstanley, Bulk emission of scalars by a rotating black hole, *JHEP* **2008** (6), 071.
- [20] J. G. Rosa and T. W. Kephart, Stimulated Axion Decay in Superradiant Clouds around Primordial Black Holes, *Phys. Rev. Lett.* **120**, 231102 (2018).
- [21] W. E. East and F. Pretorius, Superradiant Instability and Backreaction of Massive Vector Fields around Kerr Black Holes, *Phys. Rev. Lett.* **119**, 041101 (2017).
- [22] R. A. Konoplya and A. Zhidenko, Wormholes versus black holes: quasinormal ringing at early and late times, *JCAP* **2016** (12), 043.
- [23] M. Richartz, A. Prain, S. Liberati, and S. Weinfurter, Rotating black holes in a draining bathtub: Superradiant scattering of gravity waves, *Phys. Rev. D* **91**, 124018 (2015).
- [24] M. Wang and C. Herdeiro, Maxwell perturbations on Kerr-anti-de Sitter black holes: Quasinormal modes, superradiant instabilities, and vector clouds, *Phys. Rev. D* **93**, 064066 (2016).
- [25] H. Yoshino and H. Kodama, Gravitational radiation from an axion cloud around a black hole: Superradiant phase, *PTEP* **2014**, 043E02 (2014).
- [26] C.-Y. Zhang, S.-J. Zhang, P.-C. Li, and M. Guo, Superradiance and stability of the regularized 4D charged Einstein-Gauss-Bonnet black hole, *JHEP* **2020** (8), 105.

- [27] S. C. Sun and Y. L. Zhang, Fast gravitational wave bursts from axion clumps, *Phys. Rev. D* **104**, 103009 (2021).
- [28] N. Aggarwal, O. D. Aguiar, and A. Bauswein, Challenges and opportunities of gravitational-wave searches at MHz to GHz frequencies, *Living Rev. Rel.* **24**, 4 (2021).
- [29] S. Endlich and R. Penco, A modern approach to superradiance, *JHEP* **2017** (5), 52.
- [30] V. Cardoso, A. Coutant, M. Richartz, and S. Weinfurter, Detecting Rotational Superradiance in Fluid Laboratories, *Phys. Rev. Lett.* **117**, 271101 (2016).
- [31] A. A. Starobinsky, Amplification of waves reflected from a rotating "black hole", *Sov. Phys. JETP* **37**, 28 (1973).
- [32] J. D. Bekenstein and M. Schiffer, The many faces of superradiance, *Phys. Rev. D* **58**, 064014 (1998).
- [33] D. Faccio and E. M. Wright, Superradiant amplification of acoustic beams via medium rotation, *Phys. Rev. Lett.* **123**, 044301 (2019).
- [34] T. Torres, S. Patrick, A. Coutant, M. Richartz, E. W. Tedford, and S. Weinfurter, *Nat. Phys.* **13**, 833 (2017).
- [35] N. Andersson, P. Laguna, and P. Papadopoulos, Dynamics of scalar fields in the background of rotating black holes. 2. A Note on superradiance, *Phys. Rev. D* **58**, 087503 (1998), arXiv:gr-qc/9802059.
- [36] V. L. Ginzburg and I. M. Frank, *J. Phys. (USSR)* **9**, 353 (1945).
- [37] V. Cardoso and S. Yoshida, Superradiant instabilities of rotating black branes and strings, *JHEP* **07**, 009, arXiv:hep-th/0502206.
- [38] P. M. Saffin, Q. X. Xie, and S. Y. Zhou, Q-Ball Superradiance, *Phys. Rev. Lett.* **131**, 111601 (2023).
- [39] D. Yang, S. Oh, J. Han, G. Son, J. Kim, J. Kim, M. Lee, and K. An, Realization of superabsorption by time reversal of superradiance, *Nat. Photon.* **15**, 272 (2021).
- [40] J. Kim, S. Oh, D. Yang, J. Kim, M. Lee, and K. An, A photonic quantum engine driven by superradiance, *Nat. Photon.* **16**, 707 (2022).
- [41] M. Jeon, J. Kim, and K. An, Numerical analysis of a superradiance-sideband-assisted laser with a zero frequency pulling and a narrow linewidth, (2024), arXiv:2408.09486 [quant-ph].
- [42] J. F. Nye and M. V. Berry, Dislocations in wave trains, *Proc. R. Soc. Lond. A* **336**, 165 (1974).
- [43] K. Volke-Sepúlveda, A. O. Santillán, and R. R. Boullosa, Transfer of angular momentum to matter from acoustical vortices in free space, *Phys. Rev. Lett.* **100**, 024302 (2008).
- [44] M. Croom, G. M. Gibson, E. Toninelli, M. J. Padgett, E. M. Wright, and D. Faccio, Amplification of waves from a rotating body, *Nat. Phys.* **16**, 1069 (2020).
- [45] G. M. Gibson, E. Toninelli, S. A. R. Horsley, G. C. Spalding, E. Hendry, D. B. Phillips, and M. J. Padgett, Reversal of orbital angular momentum arising from an extreme Doppler shift, *PNAS* **15**, 3800 (2018).
- [46] J. Courtial, K. Dholakia, D. A. Robertson, L. Allen, and M. J. Padgett, Measurement of the rotational frequency shift imparted to a rotating light beam possessing orbital angular momentum, *Phys. Rev. Lett.* **80**, 3217 (1998).
- [47] K. D. Skeldon, C. Wilson, M. Edgar, and M. J. Padgett, An acoustic spanner and its associated rotational doppler shift, *New J. Phys.* **10**, 013018 (2008).
- [48] M. P. J. Lavery, F. C. Speirits, S. M. Barnett, and M. J. Padgett, Detection of a spinning object using light's orbital angular momentum, *Science* **341**, 537 (2018).
- [49] C. Rosales-Guzmán, N. Hermosa, A. Belmonte, and J. P. Torres, Dislocations in wave trains, *Sci. Rep.* **3**, 2815 (2013).
- [50] D. B. Phillips, M. P. Lee, F. C. Speirits, S. M. Barnett, S. H. Simpson, M. P. J. Lavery, M. J. Padgett, and G. M. Gibson, Rotational doppler velocimetry to probe the angular velocity of spinning microparticles, *Phys. Rev. A* **90**, 011801 (2014).
- [51] S. A. Teukolsky and W. H. Press, Perturbations of a rotating black hole. III. Interaction of the hole with gravitational and electromagnetic radiation., *Astrophys. J.* **193**, 443 (1974).
- [52] W. Press and S. Teukolsky, Floating Orbits, Superradiant Scattering and the Black-hole Bomb., *Nature* **238**, 211 (1972).
- [53] V. Cardoso, O. J. C. Dias, J. P. S. Lemos, and S. Yoshida, The Black hole bomb and superradiant instabilities, *Phys. Rev. D* **70**, 044039 (2004), arXiv:hep-th/0404096.
- [54] P. Pani, V. Cardoso, L. Gualtieri, E. Berti, and A. Ishibashi, Black-Hole Bombs and Photon-Mass Bounds, *Phys. Rev. Lett.* **109**, 131102 (2012).
- [55] J. C. Degollado and C. A. R. Herdeiro, Time evolution of superradiant instabilities for charged black holes in a cavity, *Phys. Rev. D* **89**, 063005 (2014).
- [56] O. J. C. Dias and R. Masachs, Charged black hole bombs in a Minkowski cavity, *Class. Quant. Grav.* **35**, 184001 (2018).
- [57] S. Hod, Analytic treatment of the charged black-hole-mirror bomb in the highly explosive regime, *Phys. Rev. D* **88**, 064055 (2013).
- [58] R. Li, J. K. Zhao, and Y. M. Zhang, Superradiant Instability of D-Dimensional Reissner—Nordström Black Hole Mirror System, *Commun. Theor. Phys.* **63**, 569 (2015).
- [59] M. Visser, Acoustic black holes: horizons, ergospheres and hawking radiation, *Class. Quant. Grav.* **15**, 1767 (1998).
- [60] E. Berti, V. Cardoso, and J. P. S. Lemos, Quasinormal modes and classical wave propagation in analogue black holes, *Phys. Rev. D* **70**, 124006 (2004), arXiv:gr-qc/0408099.
- [61] V. Cardoso, J. P. S. Lemos, and S. Yoshida, Quasinormal modes and stability of the rotating acoustic black hole: Numerical analysis, *Phys. Rev. D* **70**, 124032 (2004), arXiv:gr-qc/0410107.
- [62] S. Lepe and J. Saavedra, Quasinormal modes, superradiance and area spectrum for 2+1 acoustic black holes, *Phys. Lett. B* **617**, 174 (2005), arXiv:gr-qc/0410074.
- [63] M. Mironov, Propagation of a flexural wave in a plate whose thickness decreases smoothly to zero in a finite interval, *Sov. Phys. Acoust.* **34**, 318 (1988).
- [64] S. W. Hawking, Black hole explosions?, *Nature* **248**, 30 (1974).
- [65] S. W. Hawking, Particle creation by black holes, *Commun. math Phys.* **46**, 206 (1976).
- [66] S. W. Hawking, Breakdown of predictability in gravitational collapse, *Phys. Rev. D* **14**, 2460 (1976).
- [67] M. K. Parikh and F. Wilczek, Hawking Radiation As Tunneling, *Phys. Rev. Lett.* **85**, 5042 (2000).
- [68] S. Hemming and E. Keski-Vakkuri, Hawking radiation from AdS black holes, *Phys. Rev. D* **64**, 044006 (2001).
- [69] V. V. Krylov, Surface effects and surface acoustic waves., *Prog. Surf. Sci.* **32**, 39 (1989).
- [70] V. V. Krylov and F. J. B. S. Tilman, Acoustic 'black holes' for flexural waves as effective vibration dampers,

- J. Sound Vib. **274**, 605 (2004).
- [71] V. Denis, A. Pelat, F. Gautier, and B. Elie, Modal overlap factor of a beam with an acoustic black hole termination, J. Sound Vib. **333**, 2475 (2014).
- [72] L. Tang and L. Cheng, Enhanced acoustic black hole effect in beams with a modified thickness profile and extended platform, J. Sound Vib. **391**, 116 (2017).
- [73] A. Pelat, F. Gautier, S. C. Conlon, and F. Semperlotti, The acoustic black hole: A review of theory and applications, J. Sound Vib. **476**, 115316 (2020).
- [74] F. Cheli and G. Diana, Introduction to the finite element method, in *Advanced Dynamics of Mechanical Systems* (Springer International Publishing, Cham, 2015) pp. 311–412.
- [75] O. C. Zienkiewicz, R. L. Taylor, and J. Z. Zhu, The finite element method: Its basis and fundamentals (2005).
- [76] COMSOL, COMSOL Multiphysics Modeling Software .
- [77] A. D. Pierce and R. T. Beyer, Acoustics: An Introduction to Its Physical Principles and Applications, J. Acoust. Soc. Am. **87**, 1826 (1990).
- [78] S. W. Rienstra and A. Hirschberg, An Introduction to Acoustics .
- [79] M. E. Delany and E. N. Bazley, Acoustical properties of fibrous absorbent materials, Appl. Acoust. **3**, 105 (1970).
- [80] M. Yasushi, Acoustical properties of porous materials-modifications of delany-bazley models-, J. Acoust. Soc. Jpn. (E) **11**, 19 (1990).
- [81] P. M. Fridolin, Formulas of Acoustics. (2004).